nature astronomy

SUPPLEMENTARY INFORMATION
https://doi.org/10.1038/s41550-017-0289-8

In the format provided by the authors and unedited.

Powering prolonged hydrothermal activity inside Enceladus

Gaël Choblet[1*], Gabriel Tobie[1], Christophe Sotin[2], Marie Běhounková[3], Ondřej Čadek[3], Frank Postberg[4,5] and Ondřej Souček[6]

[1]Laboratoire de Planétologie et Géodynamique, UMR-CNRS 6112, Université de Nantes, 44322 Nantes Cedex 03, France. [2]Jet Propulsion Laboratory, Caltech, 4800 Oak Grove Drive, Pasadena, CA 91109, USA. [3]Charles University, Department of Geophysics, V Holešovičkách 2, 180 00 Praha 8, Czech Republic. [4]Institut für Geowissenschaften, Universität Heidelberg, Im Neuenheimer Feld 236, 69120 Heidelberg, Germany. [5]Klaus-Tschira-Labor für Kosmochemie, Universität Heidelberg, Im Neuenheimer Feld 236, 69120 Heidelberg, Germany. [6]Charles University, Mathematical Institute, Sokolovská 83, 186 75 Praha 8, Czech Republic. *e-mail: gael.choblet@univ-nantes.fr

Supplementary Information to "Powering prolonged hydrothermal activity inside Enceladus"

September 11, 2017

S1 Results for tidal deformation in Enceladus' interior

Supplementary Figure 1 shows the values of Love number k_2 evaluated classically on the surface and global dissipation factor, Q corresponding to the global dissipation shown in Fig. 1-A. Note that for a very dissipative core (0.2< Q_μ^{-1} <0.8), the global dissipation function ($1/Q$) ranges between 0.1 and 0.5, corresponding to a time lag between ∼0.5 and 2.5 h. Such a dissipative core may explain part of the 4-5 h time lag inferred from the delayed plume activity[1,2,3], but it is probably not the only source of delayed response.

Supplementary Figure 2-A displays the effective cyclic strain corresponding to the heating rate profile displayed in Figure 1-B at the pole and equator. The heating rate and cyclic strain displayed on Supplementary Figure 2-A have been computed assuming a constant ice shell thickness equal to 20 km at both equator and pole and an ice viscosity of 10^{18} Pa s. Tests performed with ice shell thickness varying between 50 and 10 km showed that the cyclic strain and heating rate in the core is not sensitive to the ice shell thickness, at least for this range of thickness. The difference between the equator and the pole is mostly controlled by the pattern of the tidal potential. The amplitudes of cyclic strain and tidal heating at both equator and pole are mostly controlled by the assumed values of $\mu_{\rm eff}$ and Q_μ^{-1}, which have been fixed to 1.6×10^7 Pa and 0.5, respectively for the results displayed on Supplementary Figure 2-A, corresponding to a total power of about 20 GW. The modulus of the complex Love number, k_2, and the global dissipation factor, Q, corresponding to these computations are displayed in Supplementary Table 4 . The amplitude of cyclic strain is mostly determined by the assumed effective shear modulus, while the heating rate is determined by the combination of dissipation function and effective shear modulus. Supplementary Figure 2-A also displays the curves computed at the equator for a model with no internal ocean, assuming the same core properties. This illustrates that the mechanical coupling between the ice shell and the core results in a dramatic decrease of heating rate by more than one order of magnitude.

In order to search for possible differences between the South Pole and the North Pole, we test the influence of the ice shell deformation on the core deformation. Supplementary Figure 2-B compares two examples of computation performed for different assumptions for the ice shell properties, and assuming the same core properties as in Supplementary Figure 2-A. The North Pole context is represented by an ice shell thickness of 15 km with a constant viscosity of 10^{18} Pa.s. For the South Pole, an ice shell thickness equal to 3 km is considered as well as a very low viscosity set to 10^{13} Pa.s inducing an increase of tidal deformation. Note that an equivalent result is obtained if, alternatively, the value of the shear modulus is reduced to 0.3 GPa. This more deformable ice shell results in an increase of core tidal heating by a factor of 2 at the South Pole relative to the North Pole which suggests that the pattern displayed in Figure 1-C of the main text should be asymmetric between the South pole and the North pole. A positive feedback is thus to be expected between the ice shell thickness at the South Pole and the amplitude of the hotspot at the seafloor in this region. Furthermore, once major faults have formed in a thin ice shell, tidal dissipation along these will get amplified as the shell thins further[4], which would further enhance the feedback, thus possibly explaining the thermal runaway observed at the South pole. However, determining the exact consequences of variations in ice shell thickness and mechanical properties on the core deformation would require a full 3D approach, similar to Souček et al.[4], including the coupling between the ice shell, the ocean and the core, which is out of the scope of the present study. For this reason, we consider a pattern with equatorial symmetry in our study and only discuss qualitatively the possible consequences of variable response between the North Pole and the South Pole.

S2 Results for porous convection

Note that even for the smallest permeability value (10^{-15} m^2), all the models investigated here for porous convection present supercritical convective states: the Rayleigh number γ typically ranges between 30 and 3×10^4 for an increasing value of K in the range 10^{-15}-10^{-12} m^2 (although not strictly comparable due to different set-ups, the critical Rayleigh number for a Cartesian, bottom heated layer with constant fluid properties[9] is $4\pi^2$).

S2.1 An example calculation - K=10^{-13} m^2, $P_{\rm tide}$=30 GW (heterogeneous heating), ϕ=0.2

Supplementary Figure 4 and Supplementary Figure 5 display the typical temporal evolution and the final radial profiles obtained for a specific calculation. This case leads to a weakly time-dependent solution: both the final thermal state and the final flow field are reached within less than 300 Myr in this case. Polygons formed by upwelling sheets nevertheless keep evolving after the steady-state is reached: lateral drift of these features, merging of adjacent polygons (see also pattern in Supplementary Figure 7 and Fig. 3 in the main text).

Radial profiles (Supplementary Figure 5) provide a good illustration of the typical transfer mechanism of the porous flow described in the main text: slow (passive) motion of cold water entering the core, gradual heating of these broad water volumes and faster (active) ascent through focused upwellings. Other than the velocity profiles, the respective volumes associated with upwellings/downwellings explain the proximity between the average profile and the cold/downwelling profiles for temperature. Radial advection is predominant in this case (three times larger than diffusion at the ocean/core interface).

S2.2 Two numerical tests

The two bottom rows in Supplementary Figure 5 also demonstrate that : 1) the resolution of our calculations is adapted (middle row): in all calculations, the grid mesh includes six blocks with 64 uniformly spaced cells in the r direction (corresponding to a radial increment of 2.3 km) and 64 in the two lateral directions (corresponding to an average grid spacing of 4.5 km at the surface of the core and 0.9 km on the inner boundary); doubling the number of cells in the three spatial directions (with a grid mesh size 6×128^3) does not modify drastically the results even in one of the most challenging cases depicted here; 2) the choice to neglect heat diffusion in the regions where heat advected in the core neither alters the global solution (bottom row) besides introducing a sharp boundary layer at the surface whose resolution is more challenging - even in this example where the mesh size is again doubled in the three directions, one may wonder whether the resolution is sufficient. Note that for these last two rows, the largest difference with the reference profiles is observed for the passive downwelling velocity (blue curves and dotted lines in Supplementary Figure 5-h,m). We suspect part of this (unimportant) difference can be caused by a too short time averaging period for these two demanding runs.

S2.3 Synthetic results

Supplementary Figure 6 and Supplementary Figure 7 summarize the entire set of calculations (except for a few additional cases with $P_{\rm tide}$=50 GW). All calculations are run to a statistical steady state. For cases with a homogeneous heating, the initial condition is a uniform temperature corresponding to the surface value (273 K) with a spherical harmonic perturbation (the wavelength and amplitude of which is found to have no effect on the steady-state equilibrium solution even in cases corresponding to a stationary solution). Cases with heterogeneous tidal heating are started from the result obtained for homogeneous heating corresponding to the same parameter values ($P_{\rm tide}, K, \phi$). In the case of heterogeneous heating the same heating pattern is used for all calculations (cf. Fig. 1 in the main text) and the amplitude is scaled to meet the constraint of a prescribed value for $P_{\rm tide}$.

The effect of porosity on the temperature values is only moderate except at the lowest value for K (10^{-15} m^2). As expected however, it has a first order impact on the flow: velocity values obtained for $\phi = 0.1$ and $P_{\rm tide}$=10 GW are always comparable to (or larger than) values for $\phi = 0.2$ and $P_{\rm tide}$=30 GW.

The global thermal structure of our results agree with the models of Travis and Schubert (2015)[7] where the parameter ranges overlap, even though the nature of numerical experiments is slightly different (e.g. theirs prescribe the effect of a varying ice shell thickness restricted to a 2D geometry, while heat focusing at the poles results from heterogenous tidal heating in our case). The base case model of Travis and Schubert (2015), corresponds to a tidal power oscillating between 10 and 15 GW and their choice for the range of permeability values, dictated by an analogy with silty sands/sandy silts is 10^{-13}-10^{-12} m^2. Porosity is 10 % in their case. These values are included in the wider range considered here. If K=10^{-13} m^2, the peak temperature in their base case is 15^{o}C to be compared to the range 7^{o}C (33^{o}C) for the average (maximum) temperatures in our models. If K=10^{-12} m^2, the peak temperatures is $\simeq$50^{o}C to be compared to the range 20^{o}C (80^{o}C) for the average (maximum) temperatures in our models. We note that (probably due to our 3D geometry), upwellings are more focussed in our models which likely explains the slightly higher maximum values observed in our numerical experiments.

While it has a drastic consequence on the flow pattern, the introduction of heterogeneous heating does not alter significantly the average values obtained for the flow or the thermal state. Nevertheless cases with heterogeneous heating are associated with slightly larger maximum temperatures in hot upwellings (especially at lower K values) and slightly larger maximum upwelling velocities (especially at larger K values).

Supplementary Figure 8 focuses specifically on the heat budget: while the net power output in a steady-state is dictated by (and equal to) the value of the tidal power $P_{\rm tide}$:

$$P_{\rm out} + P_{\rm dif} = P_{\rm in} + P_{\rm tide} \tag{1}$$

with $P_{\rm in}$/$P_{\rm out}$ the heat power advected in/out of the core, respectively, and $P_{\rm dif}$ the power extracted from the core by thermal diffusion. It must be noted that the advective flux of hot water expelled from the core $P_{\rm out}$ is potentially much larger: while it has the same order of magnitude as $P_{\rm tide}$ for K=10^{-15} m^2, it is an order of magnitude larger for K=10^{-12} m^2. Diffusion of heat out the core ($P_{\rm dif}$) is always smaller than $P_{\rm tide}$ but again its role is variable: negligible for K=10^{-12} m^2, it is comparable to advection in the case K=10^{-15} m^2 and $P_{\rm tide}$=3 GW.

In our models, the mass flux $M_{\rm in}$ through the ocean/core interface is typically 10^{12} kg/yr indicating that a liquid water volume corresponding to the whole content of the ocean would be recycled in the porous core in about 25 Myr. The largest values for this mass flux are obtained for the largest permeability values ($M_{\rm in}$ ranges between 6×10^{11} and 2.5×10^{12} kg/yr for K=10^{-12} m^2 when $P_{\rm tide}$ varies between 3 and 30 GW). In this case however, the heating of liquid water in the core is very modest with maximum temperatures never exceeding 363 K. The potential to develop efficient aqueous alteration processes is maximum for permeability values in the range 10^{-14}-10^{-13} m^2 still corresponding to a large flux of liquid water ($> 10^{11}$ kg/yr).

S2.4 Hotspots at the rock core/ocean interface

Supplementary Figure 9 displays polar views of the hotspots observed at the seafloor (six specific models are considered for K=10^{-13} and 10^{-14} m^2). Hotspots (i.e. regions where temperature is higher than 363 K during a significant amount of time) are observed as long as the tidal power in the core remains larger than 10 GW. Here, a possible dichotomy between North and South poles is fortuitous: a strong durable preference for one of the hemispheres is not observed in any of the simulations. Note however that a more deformable ice shell at the South Pole (not prescribed in these models) is shown to provide a significant increase of tidal heating within the core (see section S1 above). Larger values of $P_{\rm tide}$ generally increases variability of low-latitude hotspots and polar hotspots are predominant in some models. An evolution in the hotspot pattern from linear sheets along the leading and trailing meridians to more discrete points is observed when permeability K and tidal power $P_{\rm tide}$ are increased.

References

[1] Hedman, M. M., Gosmeyer, C. M., Nicholson, P. D., Sotin, C., Brown, R. H., Clark, R. N., Baines, K.H., Buratti, B.J., Showalter, M. R., 2013. An observed correlation between plume activity and tidal stresses on Enceladus. *Nature* **500(7461)**, 182.

[2] Nimmo, F., Porco, C., Mitchell, C., 2014. Tidally modulated eruptions on Enceladus: Cassini ISS observations and models. *Astron. J.* **148(3)**, 46.

[3] Behounková, M., Tobie, G., Cadek, O., Choblet, G., Porco, C., Nimmo, F., 2015. Timing of water plume eruptions on Enceladus explained by interior viscosity structure. *Nat. Geo.* **8(8)**, 601.

[4] Souček O., Hron J., , Běhounková M., Čadek O., 2016. Effect of the tiger stripes on the deformation of Saturn's moon Enceladus. *Geophys. Res. Lett.* **43**, 7417–7423.

[5] Ricard, Y., 2015. Physics of mantle convection. In: Schubert, G. (Ed.), Mantle Dynamics. Vol. 7 of Treatise on Geophysics. Elsevier, pp. 23–71.

[6] Kalousová, K., Souček, O., Tobie, G., Choblet, G., Čadek, O., 2014. Ice melting and downward transport of meltwater by two-phase flow in Europa's ice shell. *J. Geophys. Res.* **119**, 532–549.

[7] Travis, B., Schubert, G., 2015. Keeping Enceladus warm. *Icarus* **250**, 32–42.

[8] Palme, H. O'Neill, H. S. C., 2003. Cosmochemical estimates of mantle composition. In: Carlson RW (ed.) Mantle and Core. Vol. 2 of Treatise on Geochemistry. Elsevier, pp. 1–38.

[9] Straughan, B., 2008. Stability and wave motion in porous media. Vol. 165. Springer New York.

[10] Goodman, J. C., Collins, G. C., Marshall, J., Pierrehumbert, R. T., 2004. Hydrothermal plume dynamics on Europa: Implications for chaos formation. *J. Geophys. Res.* **109**, E03008.

[11] Goodman, J. C., Lenferink, E., 2012. Numerical simulations of marine hydrothermal plumes for Europa and other icy worlds. *Icarus* **221**, 970–983.

[12] Postberg, F., Kempf, S., Schmidt, J., Brilliantov, N., Beinsen, A., Abel, B., Buck, U., Srama, R., 2009. Sodium salts in E-ring ice grains from an ocean below the surface of Enceladus, *Nature* **459**, 1098–1101.

[13] Johnson, J. W., Oelkers, E. H., Helgeson, H. C., 1992. Supcrt92: A software package for calculating the standard molal thermodynamic properties of minerals, gases, aqueous species, and reactions from 1 to 5000 bar and 0 to 1000 C. *Chem. Geol.* **18 (7)**, 899–947.

[14] Johnson, J. W., Norton, D., 1991. Critical phenomena in hydrothermal systems; state, thermodynamic, electrostatic, and transport properties of H2O in the critical region. *Am. J. Sci.* **291 (6)**, 541–648.

parameter	symbol	value
Enceladus mass	M	$1.08\ 10^{22}$ kg
surface radius[1]	R_s	252 km
core radius[1]	R_c	186 km
ocean thickness[1]	d	47 km
ice shell density[1]	ρ_i	925 kg m^{-3}
ocean density[1]	ρ_o	1030 kg m^{-3}
core bulk thermal conductivity	k_b	2.8 W m^{-1} K^{-1}
core bulk density	ρ_b	2500 kg m^{-3}
specific heat of water	c_w	4100 J kg^{-1} K^{-1}
specific heat of rock	c_r	1000 J kg^{-1} K^{-1}
reference water density	ρ_w^0	997 kg m^{-3}
reference water viscosity	η_w^0	$8.9\ 10^{-4}$ Pa s

Supplementary Table 1: Parameters used in our Enceladus model.

mineral	formula	density (g cm^{-3})	molar mass (g)
olivine	Mg_2SiO_4	3.22	140.70
	Fe_2SiO_4	4.38	203.79
pyroxene	$Mg_2Si_2O_6$	3.20	200.79
	$Fe_2Si_2O_6$	4.00	263.88
serpentine	$Mg_3Si_2O_5\,(OH)_4$	2.58	277.09
	$Fe_3Si_2O_5\,(OH)_4$	3.29	371.73
brucite	$Mg\,(OH)_2$	2.37	58.31
	$Fe\,(OH)_2$	3.52	89.85
magnetite	Fe_3O_4	5.17	231.55

Supplementary Table 2: Densities and molar masses of the different minerals considered for modeling the porosity of Enceladus' core.

(1A)	$(\mathrm{Mg}_x\mathrm{Fe}_{1-x})_2\,\mathrm{SiO_4} + 1/2\,(\mathrm{Mg}_x\mathrm{Fe}_{1-x})_2\,\mathrm{Si_2O_6} + 2\mathrm{H_2O} \rightarrow (\mathrm{Mg}_x\mathrm{Fe}_{1-x})_3\,\mathrm{Si_2O_5}\,(\mathrm{OH})_4$
(1B)	$2\mathrm{H_2O} + 7\mathrm{O}^{2-} \rightarrow 4\mathrm{OH}^- + 5\mathrm{O}^{2-}$
(2A)	$2\,(\mathrm{Mg}_x\mathrm{Fe}_{1-x})_2\,\mathrm{SiO_4} + 3\mathrm{H_2O} \rightarrow (\mathrm{Mg}_x\mathrm{Fe}_{1-x})_3\,\mathrm{Si_2O_5}\,(\mathrm{OH})_4 + (\mathrm{Mg}_x\mathrm{Fe}_{1-x})\,(\mathrm{OH})_2$
(2B)	$3\mathrm{H_2O} + 8\mathrm{O}^{2-} \rightarrow 6\mathrm{OH}^- + 5\mathrm{O}^{2-}$
(3A)	$6\,(\mathrm{Mg_{0.75}Fe_{0.25}})_2\,\mathrm{SiO_4} + 7\mathrm{H_2O} \rightarrow 3\mathrm{Mg_3Si_2O_5}\,(\mathrm{OH})_4 + \mathrm{Fe_3O_4} + \mathrm{H_2}$
(3B)	$3\mathrm{Fe}^{2+} \rightarrow \mathrm{Fe}^{2+} + 2\mathrm{Fe}^{3+} + 2e^-$
(3C)	$7\mathrm{H_2O} + 5\mathrm{O}^{2-} + 2e^- \rightarrow 12\mathrm{OH}^- + \mathrm{H_2}$

Supplementary Table 3: Hydration of the main silicate minerals.

b_{ice} (km)	η_{ice} (Pa s)	$k_2(\times 100)$	Q
3	10^{13}	41.74	1.80
15	10^{18}	8.24	5.52
20	10^{18}	7.39	4.97
55	10^{18}	5.17	3.40
no ocean	10^{18}	1.08	75.76

Supplementary Table 4: Computed Love number k_2 and global dissipation factor Q corresponding to the models displayed in Supplementary Figure 2.

(A)

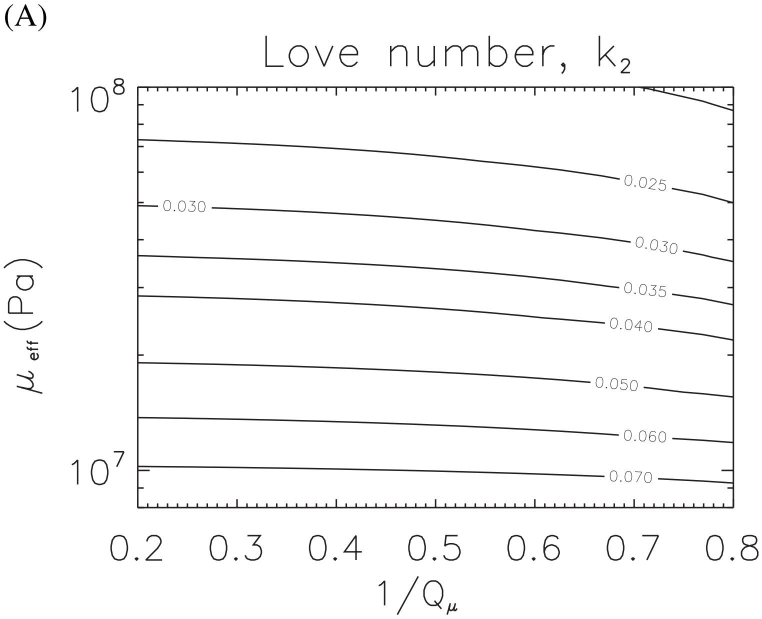

(B)

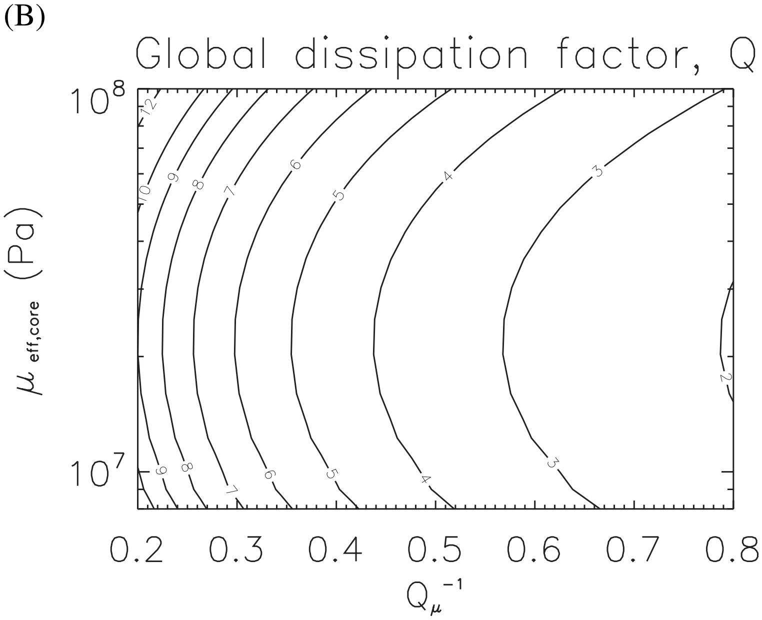

Supplementary Figure 1: **Love number k_2 (A) and global dissipation factor Q (B).**

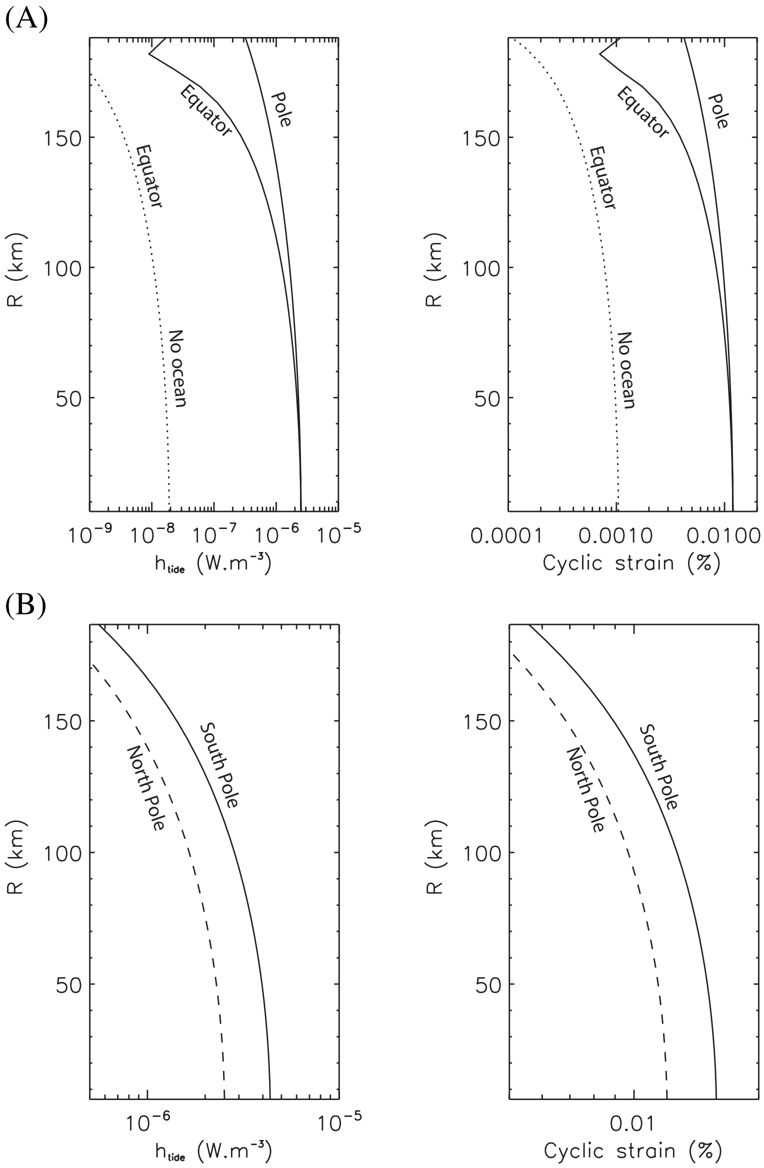

Supplementary Figure 2: **Tidal heating and cyclic strain.** (A) Profiles of tidal heating rate (left) and cyclic strain (right) in the porous core, obtained at the pole and the equator for ice shell thickness of 20 km, $\mu_{\text{eff}} = 2.5 \times 10^7$ GPa and $Q_\mu^{-1} = 0.5$. The dotted curve corresponds to the profile computed at the equator for a model with no internal ocean. (B) Profiles of tidal heating rate (left) and cyclic strain (right) in the porous core, obtained at the North Pole (dashed) and the South Pole (solid) by considering a thinner and more deformable ice shell in the south relative to the north.

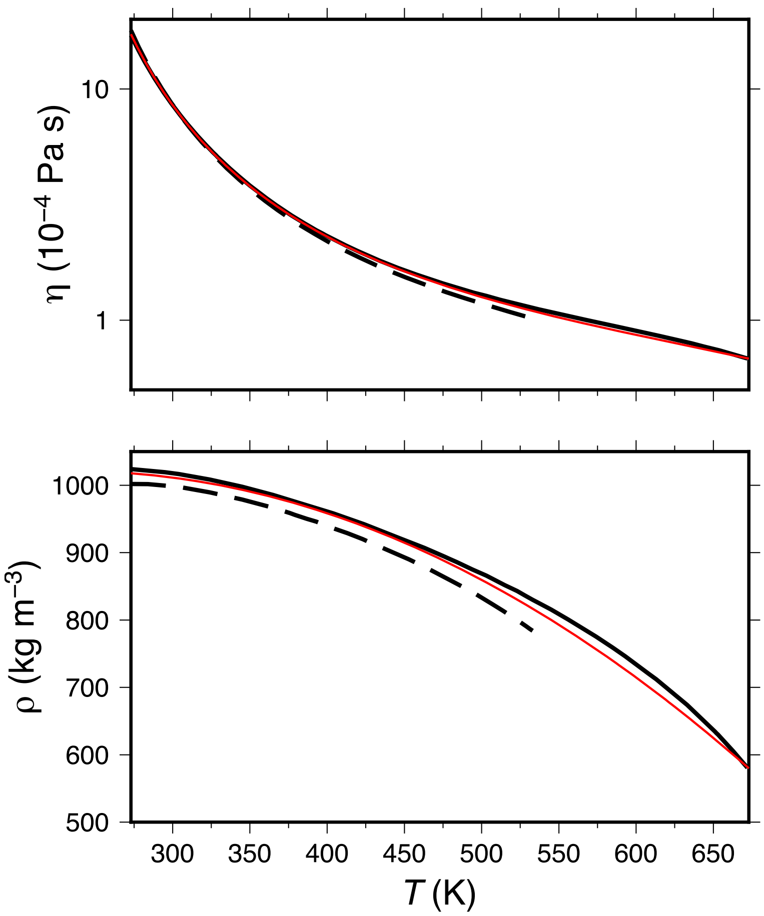

Supplementary Figure 3: **Water density and viscosity.** Values used in the present study (red) compared to the values predicted at 50 MPa (solid line) and 7 MPa (dashed line) for density[13] and for viscosity[14].

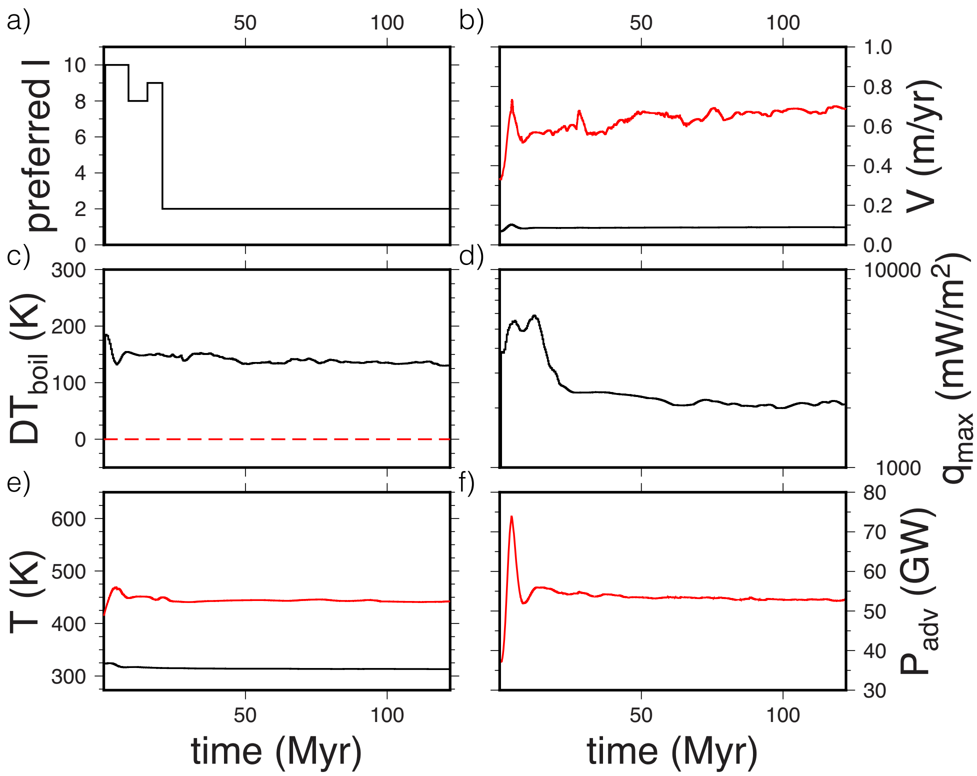

Supplementary Figure 4: **Example of a time evolution.** Case K=10^{-13} m^2, P_{tide}=30 GW (heterogeneous heating), ϕ=0.2. *a)* preferred harmonic degree for the surface heat flux; *b)* rms (black) and maximum (red) velocity; *c)* temperature difference with boiling point; *d)* maximum advective surface heat flux; *e)* average (black) and maximum (red) temperature; *f)* global power output.

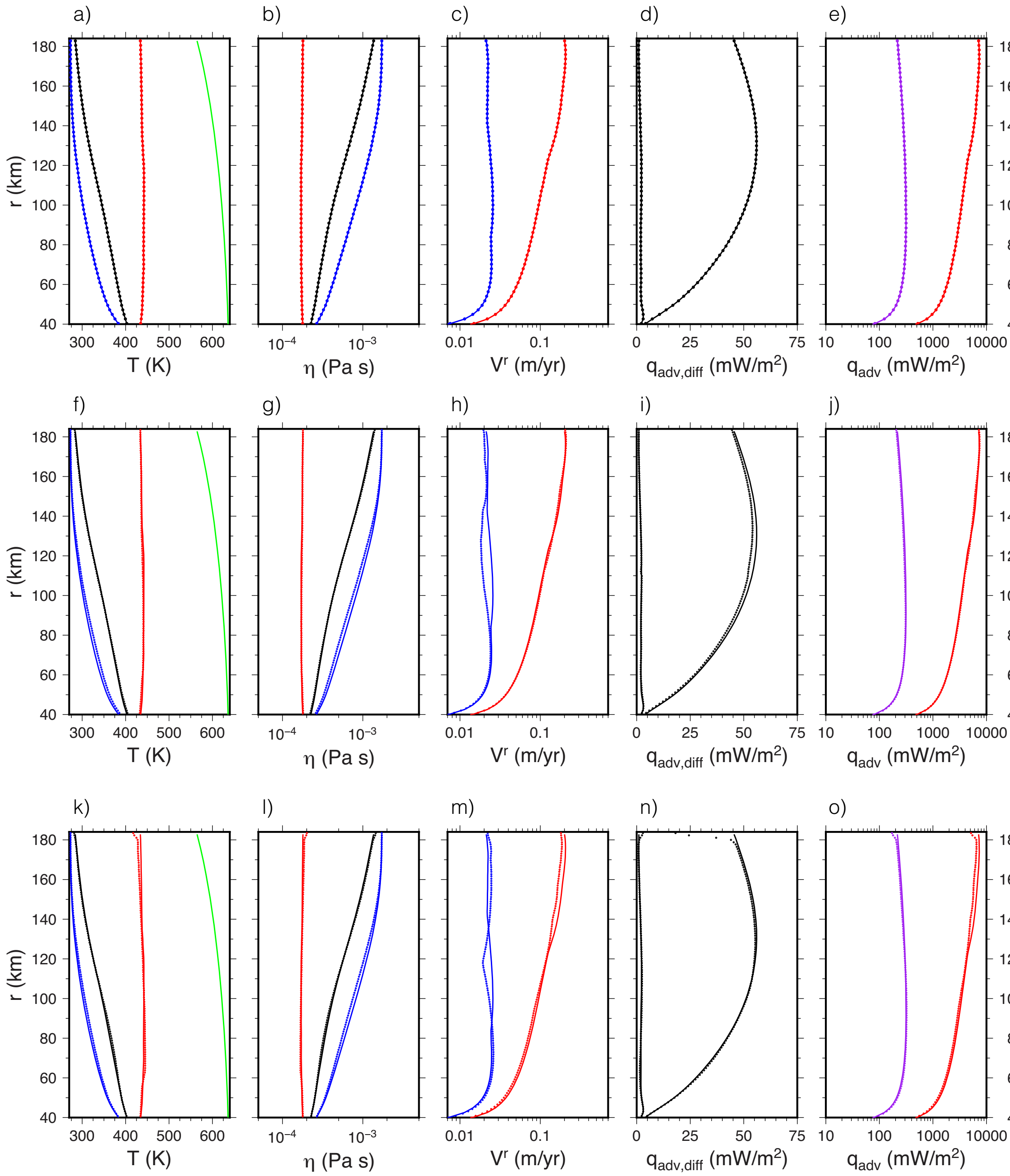

Supplementary Figure 5: **Example of time-averaged radial profiles for various numerical approximations.** Case K=10^{-13} m^2, $P_{\rm tide}$=30 GW (heterogeneous heating), ϕ=0.2. *a,f,k)* Average (black), minimum (blue) and maximum (red) temperatures as well as boiling point (green) at a given radius; *b,g,l)* liquid water viscosity; *c,h,m)* maximum upwelling (red) and downwelling (blue) flux of liquid water; *d,i,n)* radial average advective and diffusive heat flux; *e,j,o)* maximum upwelling (red) and downwelling (blue) advective flux. The top row where dotted and continuous profiles are identical, corresponds to one among the series of runs used in the present study. The same profiles also appear as a reference as solid lines on the next two rows.The middle row (dotted lines) corresponds to one test case where the spatial resolution has been doubled in the three directions (in this case, the mesh includes 6×128^3 grid cells instead of 6×64^3). The bottom row (dotted lines) corresponds to one test case where diffusion is not set to zero in the case of positive advection out of the core, contrary to all other cases presented in this study. Again, the resolution is finer in this case: 6×128^3 grid cells.

(A) homogeneous volumetric heating,

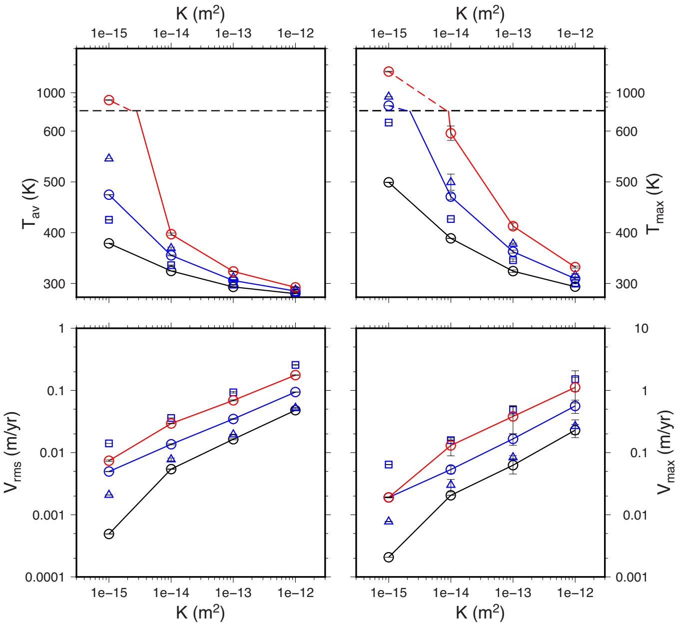

(B) heterogeneous (tidal) volumetric heating,

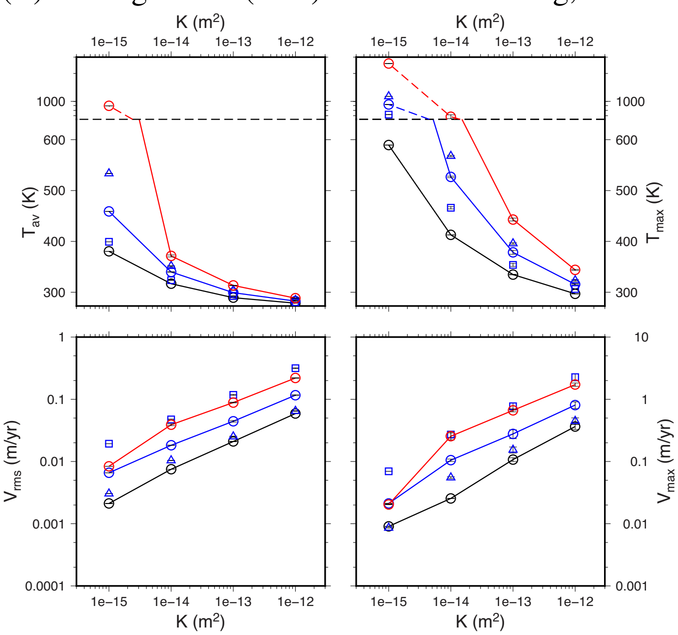

Supplementary Figure 6: **Synthetic results for the various calculations.** Average and maximum temperature (top), average and maximum radial velocity (bottom). Colours denote the global tidal power $P_{\rm tide}$: 3 GW (black), 10 GW (blue), 30 GW (red). Symbols indicate porosity ϕ: 0.1 (squares), 0.2 (circles), 0.3 (triangles). Cases with ϕ: 0.1 and 0.3 are only displayed for $P_{\rm tide}$=10 GW. Vertical "error" bars denote time-variability. Note that, in the case of temperature, two different scales (linear/log) are used with the dashed horizontal line indicating approximately the boiling point. See also Fig. 2 in the main text.

(A) homogeneous volumetric heating,

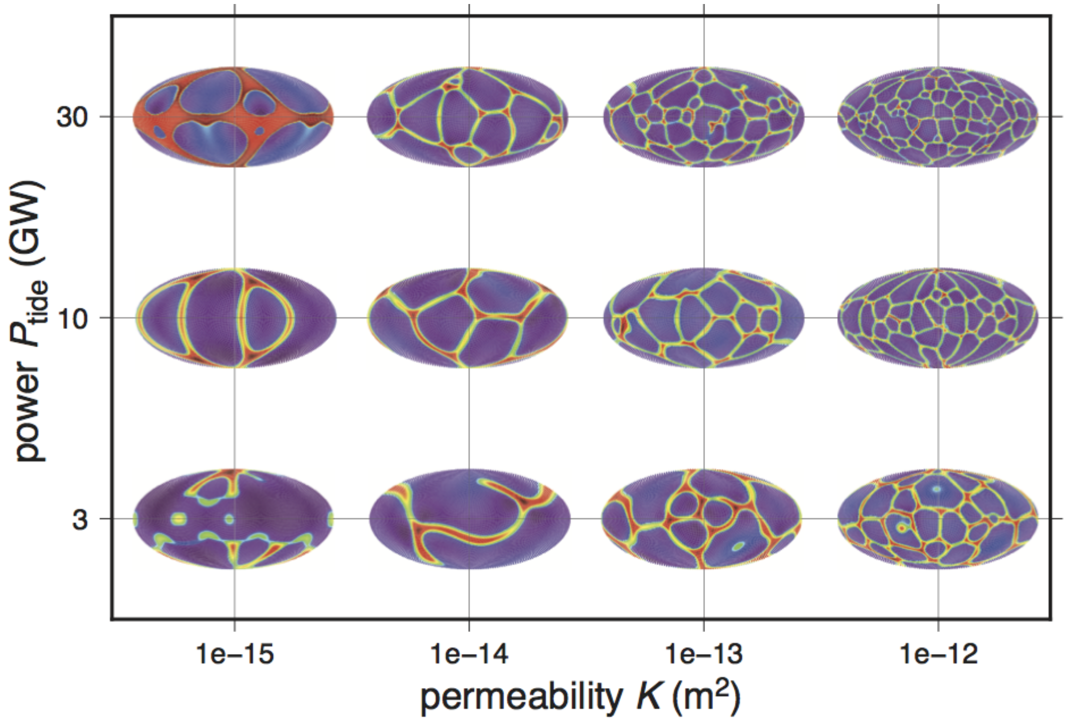

(B) heterogeneous (tidal) volumetric heating,

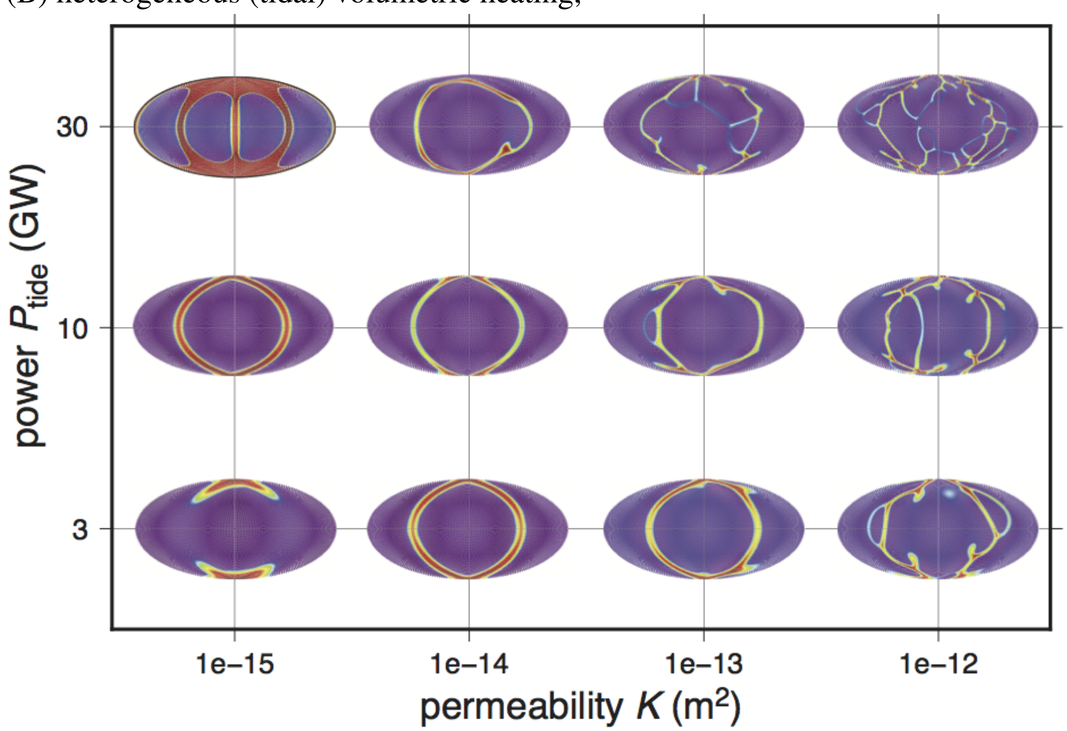

Supplementary Figure 7: **Porous flow advective heat flux through the surface.** In order to highlight the pattern, individual color scales differ among the runs (see synthetic plots above). See also Fig. 3 in the main text.

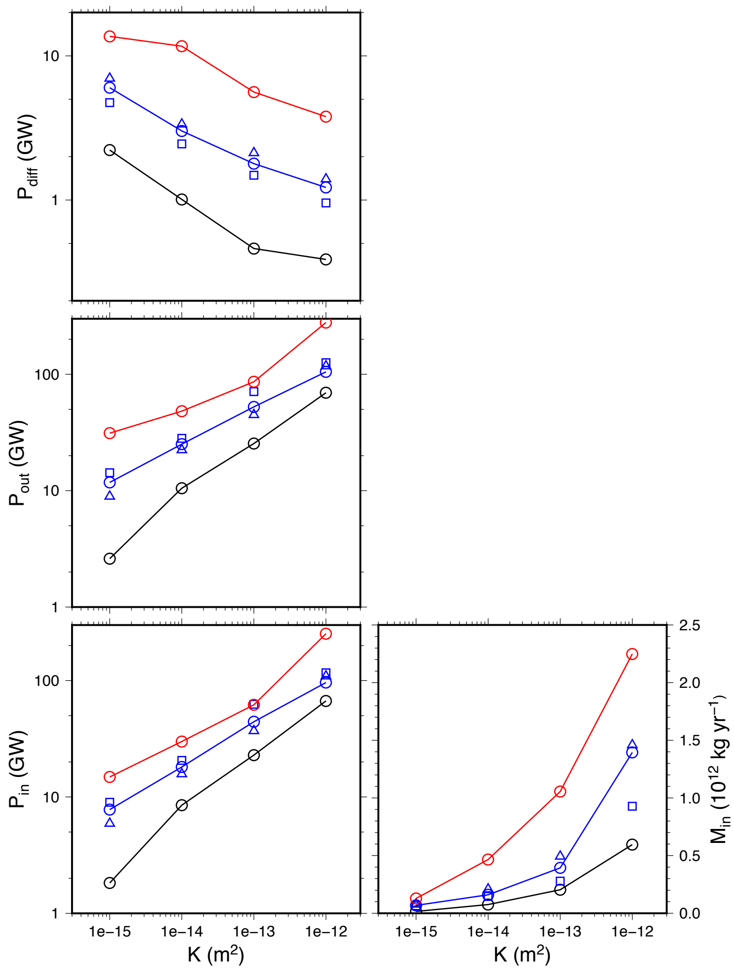

Supplementary Figure 8: **Power balance and mass flux through the ocean/core interface.** Only models with heterogeneous heating. Advection in ($P_{\rm in}$) and out ($P_{\rm out}$) of the core as well as diffusion out of the core $P_{\rm dif}$. Mass flux of liquid water $M_{\rm in}$ entering/exiting the core. Same legend as Fig. Supplementary Figure 6. Time variability is not shown here.

(A) P_{tide}=10 GW, K=10^{-13} m^2, ϕ=0.2

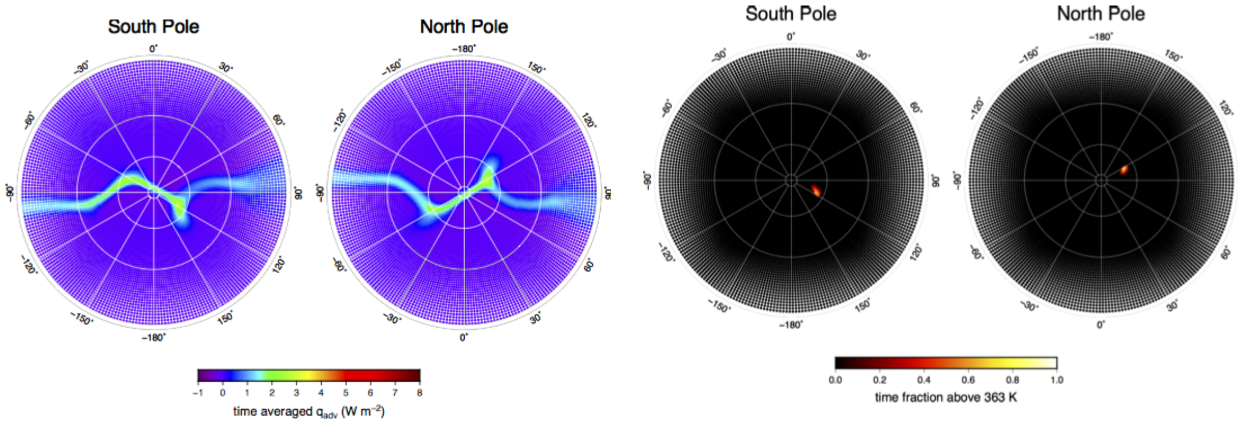

(B) P_{tide}=30 GW, K=10^{-13} m^2, ϕ=0.2

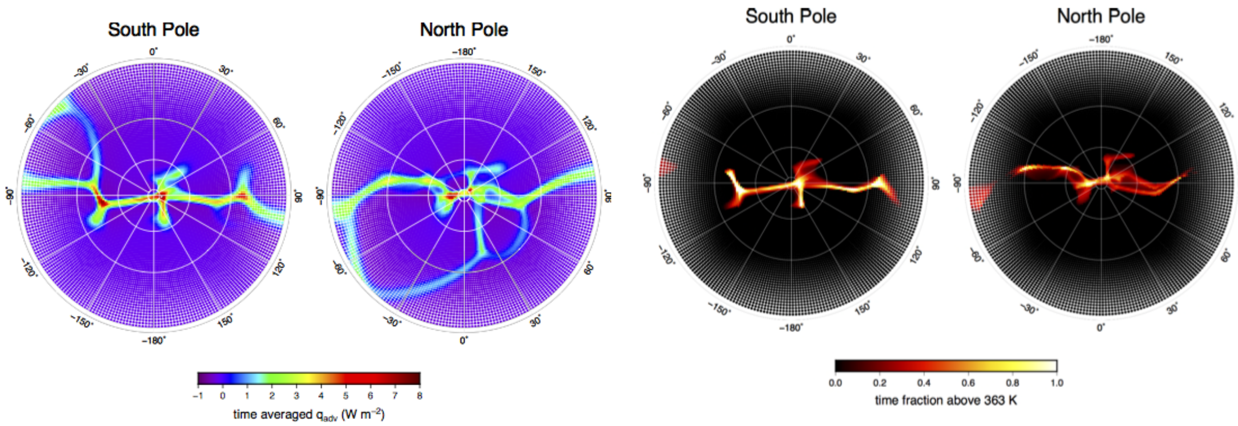

(C) P_{tide}=50 GW, K=10^{-13} m^2, ϕ=0.2

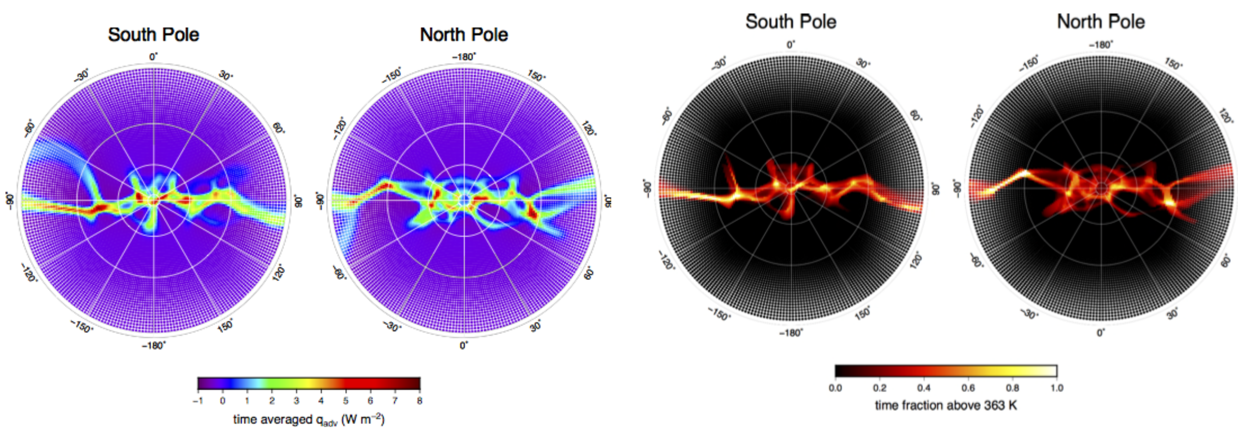

(D) P_{tide}=10 GW, K=10^{-14} m^2, ϕ=0.2

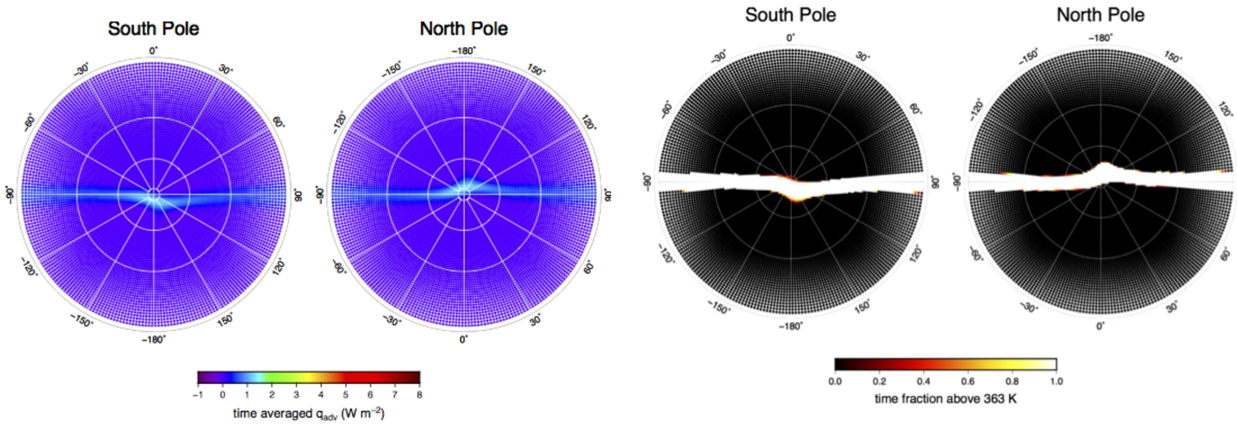

(E) P_{tide}=30 GW, K=10^{-14} m^2, ϕ=0.2

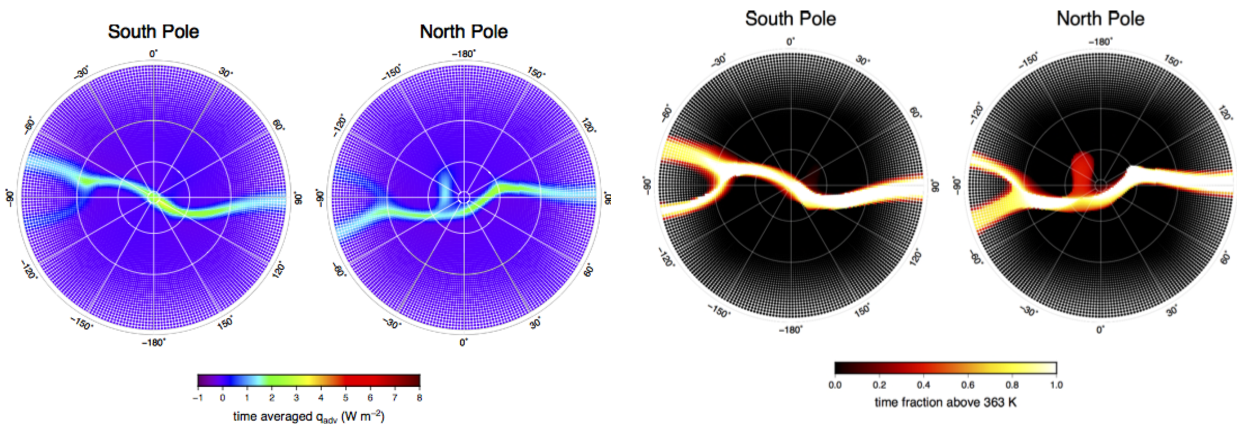

(F) P_{tide}=50 GW, K=10^{-14} m^2, ϕ=0.2

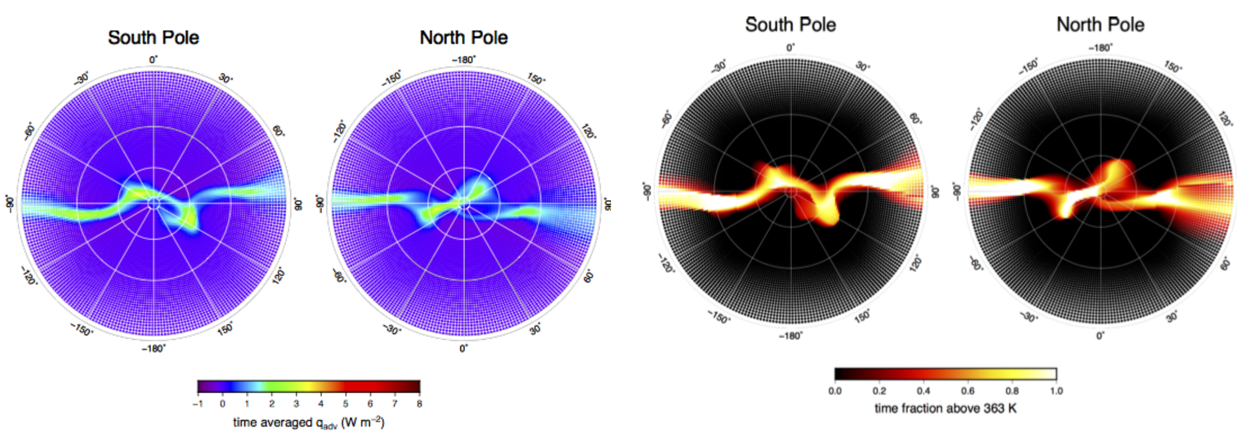

Supplementary Figure 9: **Six examples of hotspot distribution at the seafloor.** Left: instantaneous advective heat flux through the interface. Right: time fraction during which temperature at a given location remains above 363 K. The time period considered for all the calculations is 10 Myr. The color scales are identical for all six calculations. Polar stereographic projections for both hemispheres.